Supporting Information

Homeostasis in $Cu_xO/SrTiO_3$ Hybrid Allows Highly Active and Stable Visible-light Photocatalytic Performance

I. Experimental section

Materials synthesis

Untreated $SrTiO_3$ was prepared by a hydrothermal method reported in the previous work [1]. In a typical procedure of $Cu_xO/SrTiO_3$, 0.3 g untreated $SrTiO_3$ and the requisite amount of $CuSO_4$ were dispersed into 60 mL (0.2 mol L^{-1}) aqueous solution of NaOH with vigorous stirring for 30 min at room temperature to obtain a Cu_xO loading amount of 0.1, 0.5, 1.0, 2.0, 5.0 or 9.0 wt.%. Then, 3 mL (0.1 mol L^{-1}) L-ascorbic acid aqueous solution was dropwisely added into the above solution with stirring for another 30 min. The product was collected by centrifugal separation process and washed by distilled water and absolute ethanol several times. The final product was dried overnight in vacuum at 60 °C. For comparison, Cu_xO/P25 and Cu_xO/SiO_2 were prepared *via* loading 1.0 wt.% Cu_xO on P25 and SiO_2 surface respectively with the similar above fabrication process. Besides, both P25 and $SrTiO_3$ were first reduced with L-ascorbic acid before characterization and performance test as employed during the fabrication process of $Cu_xO/SrTiO_3$.

Catalysts Characterization

The morphologies and crystal analysis were obtained by transmission electron microscopy (TEM) and high-resolution TEM (HRTEM) measurements over a JEOL model JEM-2100F instrument at an accelerating voltage of 200 kV. High-angle annular dark-field (HAADF) imaging in the scanning transmission electron microscopy (STEM) mode was performed on the same electron microscope tilting the sample about a single axis using a Fischione ultra-narrow gap tomography holder. X-ray diffraction

(XRD) was performed to characterize the crystal structures and compositions of the catalysts by using a D-MAX diffractometer (Cu Kα radiation). Nitrogen adsorption/desorption isotherms at 77 K were measured by Micromeritics ASAP 2020 instrument to estimate the Brunauer-Emmett-Teller (BET) surface area, pore volume, and pore size distribution of the samples, and prior to the measurement, the samples were degassed at 573 K for 2 h. X-ray photoelectron spectroscopy (XPS) was performed using a ESCALAB 250 spectrometer (Thermo Fisher Scientific, Al K_{α}, hv = 1486.6 eV) under a vacuum of ~2×10^{-7} Pa. UV-vis diffuse reflectance spectra (DRS) were recorded on a UV-vis spectrophotometer (UV2450) with an integrating sphere attachment within the range of 200~800 nm and with $BaSO_4$ as the reflectance standard. Photoluminescence (PL) spectra were characterized by Combined Fluorescence Lifetime and Steady State Spectrometer (FLSP920) with a xenon lamp (excitation wavelength 300 nm) as a light source. Photocurrents spectra were obtained on an electrochemical analyzer (CHI660E) under visible illumination (λ = 420~780 nm) from a Xe lamp (100 mw·cm^{-2}) in a standard three-electrode system, composed of the as-prepared samples with an active area of *ca.* 2.0 cm^2 (working electrodes), Pt wire (counter electrode) and Ag/AgCl (saturated KCl) (reference electrode). The electrolyte was N_2-saturated 0.1 mol/L NaOH. The electron paramagnetic resonance (EPR) spectrometer (JESFA 200, JEOL Co.) was used for the measurements of the EPR signals of photoinduced radicals which were spin-trapped by 5,5-dimethyl-1-pyrroline-N-oxide (DMPO). The EPR signals of the DMPO trapped radicals (DMPO−•OH and DMPO−$O_2^{\bullet-}$) were recorded at ambient temperature. All freshly-prepared suspensions (DMPO: 50 mM, 20 μL; solvent: 5 mL water (for DMPO−•OH) or methanol (for DMPO−$O_2^{\bullet-}$); $m_{Catal.}$: 5 mg) were mixed directly and then transferred into a cylindrical quartz cell (length 100 mm, diameter 2 mm). A 500 W high pressure mercury lamp (λ=420~780 nm) was used *in situ* as a photo-excitation light source. After irradiation for 240 s, the signals of DMPO−•OH and DMPO−$O_2^{\bullet-}$ were measured on an EPR spectrometer.

Photocatalytic Activity Evaluation

Photocatalytic reactions were conducted in a stainless-steel reactor with a quartz window on the top, equipped with a 300 W Xe lamp with a UVIR-cut420 filter (λ = 420~780 nm, optical power density is 150 mw·cm^{-2}) under atmospheric pressure. 0.2 g photocatalyst was dispersed in a 7.0 cm^2 of quartz reaction vessel, and placed it on the bottom of the photocatalytic reactor. Then inject vaporous toluene (or benzene, xylene) to the vessel by flowing the simulated air (O_2 : N_2 = 1 : 3) into a saturator, which was filled with toluene solution. The initial toluene (or benzene, xylene) concentration was ~500 ppm, and the relative humidity in the reactor was *ca.*16%. Before irradiation, the reaction vessel was kept in dark for 30 min until achieve an adsorption–desorption equilibrium. The gas sample in the reaction vessel was withdrawn and analyzed at 30 min intervals. Besides, the action spectra for photocatalytic toluene degradation were tested under homogeneous light illumination for 2 h. The gaseous toluene (or benzene, xylene) content was test by a gas chromatograph system (GC7900, Tianmei, China) equipped with a flame ionization detector (FID), while the CO_2 formation amount was measured by another gas chromatograph (GC2060, FID), which was equipped with a nickel catalyst-based methanizer and a flame ionization detector. The performance of the photocatalyst was evaluated by the following equation:

$$Toluene\ Conversion\ \% = \frac{\left(\frac{n_{CO_2,\ t}}{7}\right)}{n_{Tol.,o}} \times 100\% \quad (1)$$

$$Benzene\ Conversion\ \% = \frac{\left(\frac{n_{CO_2,\ t}}{6}\right)}{n_{Ben.,o}} \times 100\% \quad (2)$$

$$Xylene\ Conversion\ \% = \frac{\left(\frac{n_{CO_2,\ t}}{8}\right)}{n_{Xyl.,o}} \times 100\% \quad (3)$$

Where $n_{Tol.,o}$, $n_{Ben.,o}$ and $n_{Xyl.,o}$ are the initial molar quantity of vaporous toluene, benzene and xylene in the reactor, and $n_{CO_2,\ t}$ is CO_2 molar quantity at irradiation time (t).

II. Supplementary Results

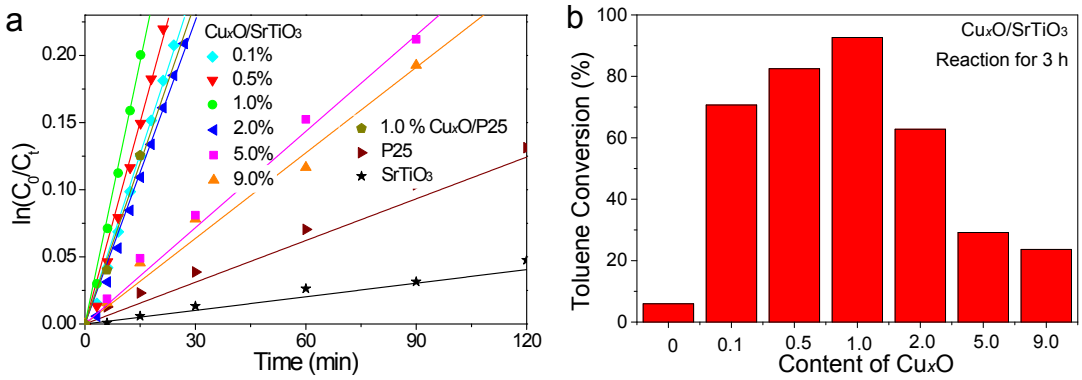

Figure S1. Visible light photocatalytic decomposition of toluene over $Cu_xO/SrTiO_3$ with different Cu_xO loadings at 30 °C: (a) $\ln(C_0/C_t)$ versus *time* plots, (b) reaction for 3 hours.

Table S1. Regressed reaction rate constants (k) and R^2 values of the photocatalytic toluene degradation over $Cu_xO/SrTiO_3$ with different Cu_xO loadings.

Samples	P25	1.0%Cu_xO/P25	$SrTiO_3$	$Cu_xO/SrTiO_3$ with different Cu_xO loadings (%)					
				0.1	0.5	1	2	5	9
K (10^{-3} min^{-1})	1.0	8.0	0.3	8.4	10.0	13.0	7.5	2.4	2.1
R^2	0.991	0.998	0.990	0.996	0.991	0.995	0.992	0.996	0.995

Table S2. The apparent reaction rate constants (k) of visible light photocatalytic toluene degradation over different photocatalysts at room temperature.

Sample	apparent rate constant(k / 10^{-3} min^{-1})	Year	Ref.
$CoCuMnO_x$	6.6	2017	2
Ho-TiO_2	6.0	2017	3
CN-STO/TN	5.4	2017	4
$ZnFe_2O_4$	2.3	2017	5
$BiVO_4$/g-C_3N_4	2.2	2017	6
Ag_3VO_4/TiO_2	7.2	2016	7
NH_2-MIL-101(Fe)	4.5	2016	8
$BiFeO_3$-$(Bi/Fe)_2O_3$	4.3	2016	9
$BiVO_4$/RGO/Bi_2O_3	0.5	2016	10
N-TiO_2	7.6	2015	11
$BiPO_4$/g-C_3N_4	7.1	2015	12
$BiVO_4$/TiO_2	6.1	2015	13
Fe_2O_3/In_2O_3	4.8	2015	14
$Ti_xZr_{1-x}O_2$	0.1	2015	15
Ag/TiO_2	8.1	2014	16
S-TiO_2	6.9	2014	17
CuO/$BiVO_4$	5.6	2014	18
V_2O_5/$BiVO_4$/TiO_2	5.5	2014	19

$Pt/SnO_2/TiO_2$	2.3	2014	20
$N\text{-}TiO_2$	8.8	2013	21
Fe_2O_3/GO	4.6	2013	22
Cu/TiO_2	3.3	2013	23
Ta_2O_5:N	1.8	2013	24
$V\text{-}TiO_2$	9.8	2012	25
$LaVO_4/TiO_2$	3.9	2012	26
$Zr/TiO_2/SiO_2$	1.1	2012	27
$BiNbO_4$:Ba	1.0	2012	28

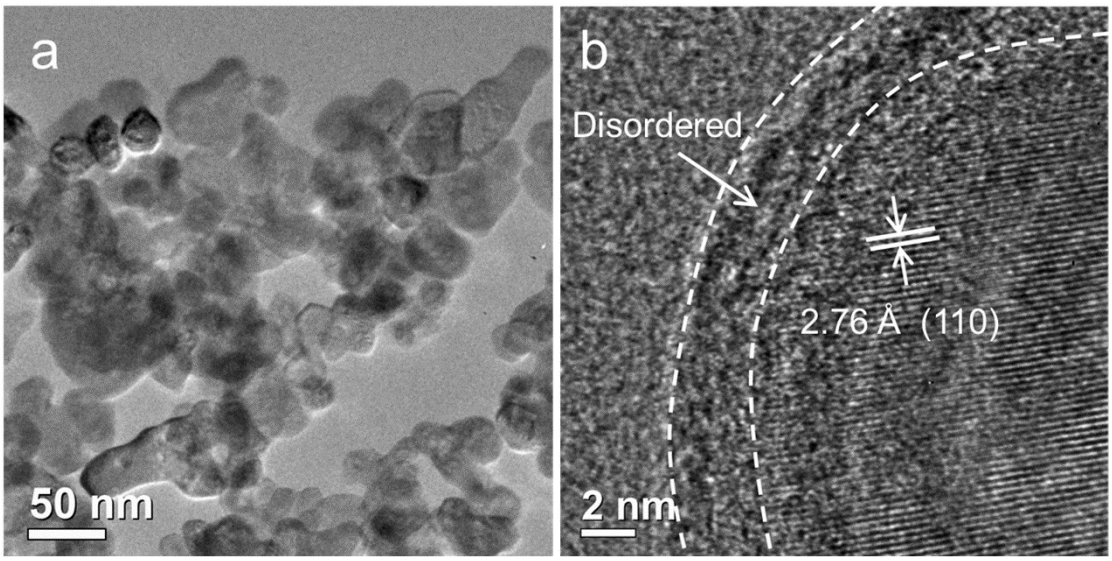

Figure S2. (a) TEM and (b) HRTEM images of $SrTiO_3$.

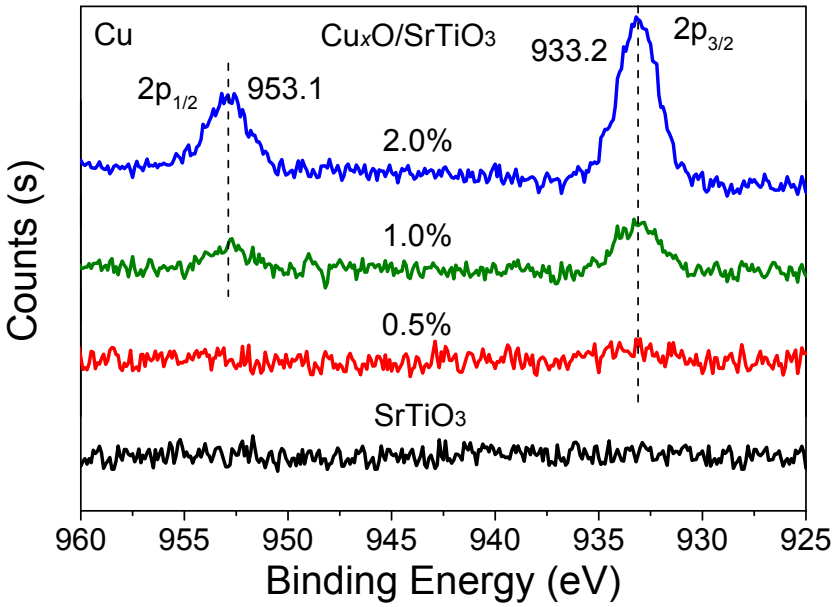

Figure S3. Cu 2p XPS spectra of the samples.

Table S3. Corresponding peak intensity ratios of Cu^{2+} (KE = 915.9 eV) to Cu^{+} (KE = 917.3 eV) in the samples.

$Cu_xO/SrTiO_3$	Cu-fresh	Cu-N_2	Cu-O_2	Cu-N_2/O_2	Cu-used
A_{Cu2+}/A_{Cu+}	0.3	0.2	0.3	0.3	0.3

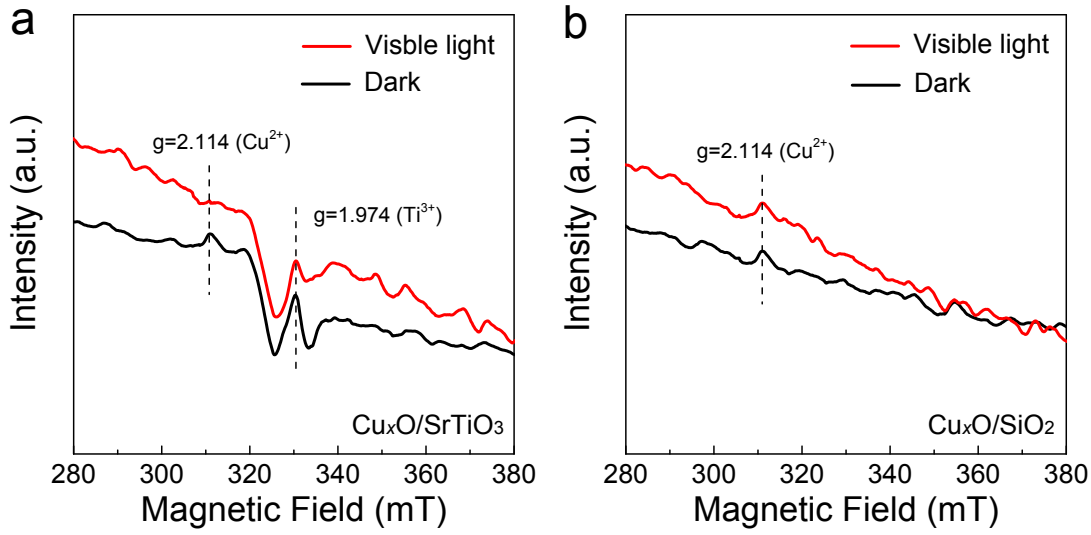

Figure S4. EPR spectra of the samples.

In order to explore the charge transport process between Cu_xO and semiconductors, Cu_xO loading on both active $SrTiO_3$ and inactive SiO_2 were prepared and characterized by EPR. As shown in **Figure S4**, $Cu_xO/SrTiO_3$ gives a strong EPR signal at g=1.974 that can be assigned to Ti^{3+} and a signal at g=2.114 arising from Cu^{2+}.[29] Under visible light irradiation, both Ti^{3+} and Cu^{2+} EPR signals weaken quickly due to the electrons transfer from Ti^{3+} to Cu^{2+} and the formation of Cu^{+} and Ti^{4+}. However, only Cu^{2+} EPR signal is detected over Cu_xO/SiO_2 and negligible difference is observed after visible irradiation, revealing no charge transport between Cu_xO and inactive SiO_2 under visible light illumination.

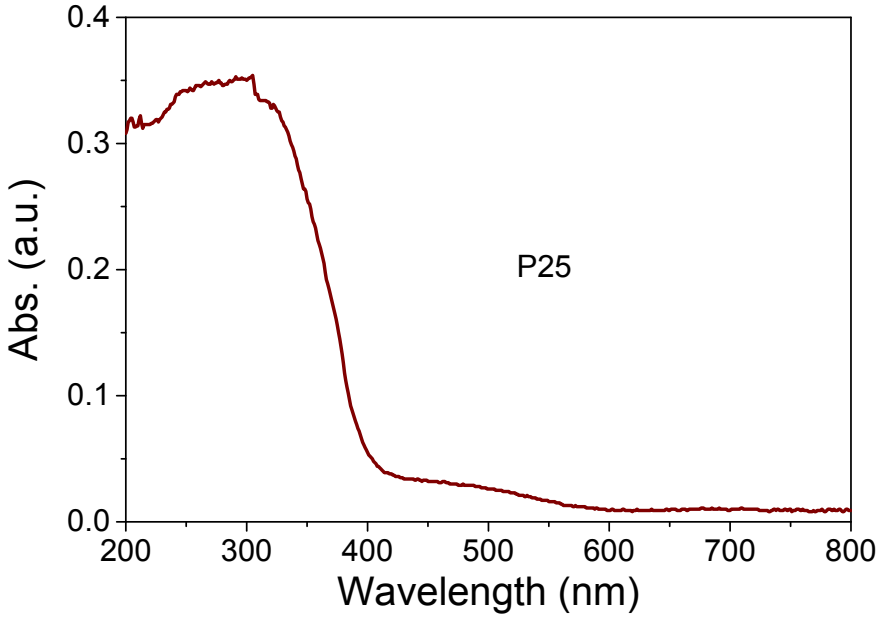

Figure S5. UV-vis diffuse reflectance spectra of P25

As displayed in **Figure S5**, the reduced P25 also show a weak absorption in visible light region due to reduction pre-treatment by L-ascorbic acid.

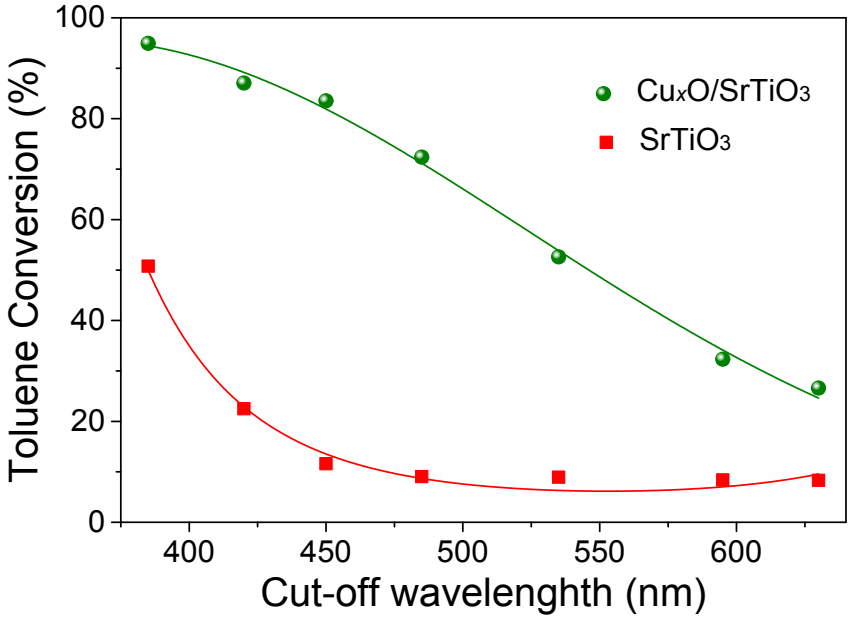

Figure S6. The action spectra of $SrTiO_3$ and $CuO_x/SrTiO_3$ for photocatalytic toluene degradation after illumination for 2 h.

Table S4. BET Surface Area (BET), Average Pore Size(d), and Pore Volume(V) of samples.

Samples	BET (m^2/g)	d^a (nm)	V^b (cm^3/g)
$SrTiO_3$	34	28	0.27
1.0% $Cu_xO/SrTiO_3$	38	18	0.17

[a]BJH Desorption average pore width. [b]BJH Desorption pore volume for the 1.7~ 300 nm range of pore diameters.

The BET surface area, average pore size and pore volume of $SrTiO_3$ and 1.0% $Cu_xO/SrTiO_3$ are listed in **Table S4**. A slight increase in BET-area and decrease in both average pore size and pore volume of upon 1.0% Cu_xO modification is probably due to the collapse of large pores and the creation of extremely small pores during the Cu_xO loading process.

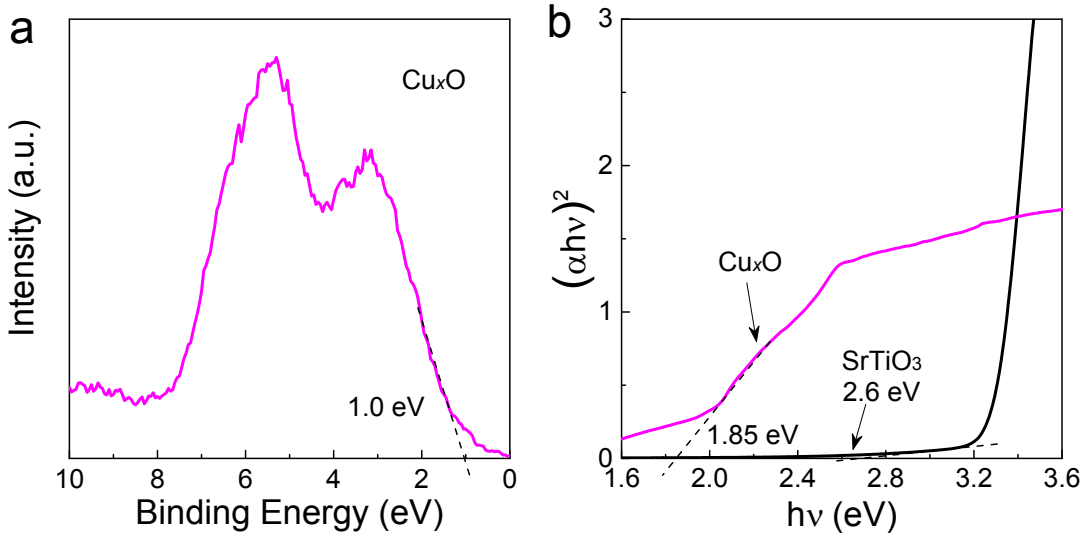

Figure S7. (a) XPS valence band spectra and (b) dependence of $(\alpha h\nu)^2$ on the photon energy for the samples. Cu_xO was prepared over SiO_2 support.

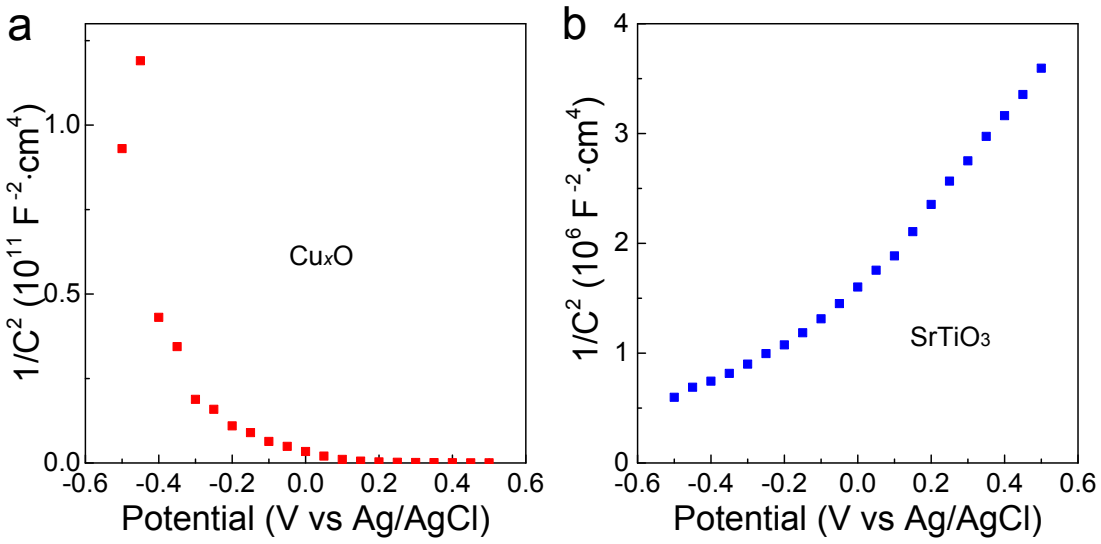

Figure S8. Mott–Schottky plots of Cu_xO (loaded on SiO_2 surface) and $SrTiO_3$

The Mott–Schottky plots of Cu_xO (loading over SiO_2 surface) and $SrTiO_3$ were shown in **Figure S8**. As presented, the Mott-Schottky curve of Cu_xO shows a negative slope, while that of $SrTiO_3$ is positive, indicating that Cu_xO is p-type semiconductor and $SrTiO_3$ is n-type.

References

1 J. J. Kong, Z. B. Rui and H. B. Ji, *Ind. Eng. Chem. Res.*, 2016, **55**, 11923-11930.

2 L. L. Bo, S. Xie, H. L. Meng, J. D. Liu and B. Gao, *Catal. Lett.*, 2017, **147**, 1623-1630.

3 P. Mazierski, W. Lisowski, T. Grzyb, M. J. Winiarski, T. Klimczuk, A. Mikolajczyk, J. Flisikowski, A. Hirsch, A. Kolakowska, T. Puzyn, A. Zaleska-Medynska and J. Nadolna, *Appl. Catal. B-Environ.*, 2017, **205**, 376-385.

4 J. J. Kong, Z. B. Rui and H. B. Ji, *Ind. Eng. Chem. Res.*, 2017.

5 H. Mehrizadeh, A. Niaei, H. H. Tseng, D. Salari and A. Khataee, *J. Photoch. Photobio. A*, 2017, **332**, 188-195.

6 R. Z. Sun, Q. M. Shi, M. Zhang, L. H. Xie, J. S. Chen, X. M. Yang, M. X. Chen and W. R. Zhao, *J. Alloy. Compd.*, 2017, **714**, 619-626.

7 X. J. Zou, Y. Y. Dong, X. D. Zhang and Y. B. Cui, *Appl. Surf. Sci.*, 2016, **366**, 173-180.

8 Z. G. Zhang, X. Y. Li, B. J. Liu, Q. D. Zhao and G. H. Chen, *RSC Adv.*, 2016, **6**, 4289-4295.

9 J. J. Kong, Z. B. Rui, X. Y. Wang, H. B. Ji and Y. X. Tong, *Chem. Eng. J.*, 2016, **302**, 552-559.

10 Q. M. Shi, W. R. Zhao, L. H. Xie, J. S. Chen, M. Zhang and Y. J. Li, *J. Alloy. Compd.*, 2016, **662**, 108-117.

11 A. M. Ferrari-Lima, R. G. Marques, M. L. Gimenes and N. R. C. Fernandes-Machado, *Catal. Today*, 2015, **254**, 119-128.
12 X. J. Zou, Y. Y. Dong, X. Y. Li, Q. D. Zhao, Y. B. Cui and G. Lu, *Catal. Commun.*, 2015, **69**, 109-113.
13 J. J. Sun, X. Y. Li, Q. D. Zhao, M. O. Tade and S. M. Liu, *J. Mater. Chem. A*, 2015, **3**, 21655-21663.
14 F. Zhang, X. Y. Li, Q. D. Zhao, Q. Z. Zhang, M. Tade and S. M. Liu, *J. Colloid Interf. Sci.*, 2015, **457**, 18-26.
15 B. J. Liu, X. Y. Li, Q. D. Zhao, J. Ke, J. Liu, S. M. Liu and M. Tade, *J. Colloid Interf. Sci.*, 2015, **438**, 1-6.
16 I. Park and S. Ko, *Nanosci. Nanotech. Let.*, 2014, **6**, 965-970.
17 W. Jo and H. Kang, *Chinese J. Catal.*, 2014, **35**, 1189-1195.
18 W. R. Zhao, W. Y. Zeng, H. P. Xi and X. X. Yu, *Acta Phys.-Chim. Sin.*, 2014, **30**, 761-767.
19 J. J. Sun, X. Y. Li, Q. D. Zhao, J. Ke and D. K. Zhang, *J. Phys. Chem. C*, 2014, **118**, 10113-10121.
20 W. R. Zhao, M. Zhang, Z. Y. Ai, Y. Yang, H. P. Xi, Q. M. Shi, X. H. Xu and H. X. Shi, *J. Phys. Chem. C*, 2014, **118**, 23117-23125.
21 J. Shie, C. Lee, C. Chiou, Y. H. Chen and C. Y. Chang, *Environ. Technol.*, 2013, **35**, 653-660.
22 H. Li, Q. D. Zhao, X. Y. Li, Z. R. Zhu, M. Tade and S. M. Liu, *J. Nanopart. Res.*, 2013, **15**.
23 W. R. ZHAO, H. P. XI and Q. W. LIAO, *Acta Phys.-Chim. Sin.*, 2013, **29**, 2232-2238.
24 R. Ullah, H. Q. Sun, H. Ang, M. Tadé and S. B. Wang, *Ind. Eng. Chem. Res.*, 2013, **52**, 3320-3328.
25 L. Laokiat, P. Khemthong, N. Grisdanurak, P. Sreearunothai, W. Pattanasiriwisawa and W. Klysubun, *Korean J. Chem. Eng.*, 2011, **29**, 377-383.
26 X. Zou, X. Li, Q. Zhao and S. Liu, *J. Colloid Interf. Sci.*, 2012, **383**, 13-18.
27 C. Kim, J. Shin, S. An, H. Jang and T. Kim, *Chem. Eng. J.*, 2012, **204-206**, 40-47.
28 R. Ullah, H. Ang, M. Tadé and S. B. Wang, *Chem. Eng. J.*, 2012, **185-186**, 328-336.
29 Y. X. Liu, B. S. Zhang, L. F. Luo, X. Y. Chen, Z. L. Wang, E. Wu, D. S. Su, and W. X. Huang, *Angew. Chem. Int. Ed.*, 2015, **54**, 15260 –15265